



OPEN

# Edge-of-chaos operation and persistent dynamics for neuromorphic meminductor computing

Abhiram Dinavahi✉ &amp; H. Rusty Harris✉

Volatile mem-elements can operate at locally active steady states thereby internally amplifying energy fluctuations. Such elements can display persistent dynamical response to a constant excitation when coupled to an appropriate passive network. While such persistent oscillations have been demonstrated for memristors, similar work for memcapacitors and meminductors is currently missing. With both elements now physically realized, their realistic models may be developed and investigated for local activity, and coupling networks which lead to persistent dynamics can be designed. This work reports the fabrication of a volatile meminductor mathematically shown to operate at the “edge-of-chaos” and presents experimental evidence of passive coupling resulting in persistent oscillatory behavior. The meminductor demonstrates quantifiable “contours of inversion (COI)” originating from state-dependent inductance, thus highlighting that complexity cannot emerge without “mem”-behavior. Finally, the coupled meminductor system has been shown to emulate second order neuronal behaviors, thus experimentally affirming the potential of meminductors in neuromorphic computing applications.

## Abbreviations

LA	Local activity/ Locally active
LP	Local passivity/ Locally passive
LU	Locally unstable
LS	Locally stable
EOC	Edge of chaos
COI	Contour of Inversion
LOI	Line of Inversion
LHP (RHP)	Left (Right) Half Plane of the complex $s$ -plane
LED	Light Emitting Diode
LDR	Light Dependent Resistor

Inherently nonlinear, two-terminal circuit elements with state-dependent electrical properties are collectively described as “mem-elements”<sup>1,2</sup> and have been widely researched over the past decade due to their in-memory-computing capabilities and rich dynamical properties<sup>3–7</sup>. Unlike linear circuit elements, volatile memelements can generate a wide array of responses to constant excitations, ranging from desirable neuron-like dynamics<sup>8–10</sup> to unwanted oscillations resulting from amplification of ambient fluctuations<sup>11</sup>. Understanding the physical mechanisms behind the origin of each such response and developing mathematical models that allow circuit designers to predictably induce selective responses while suppressing undesirable dynamics is hence crucial to unlocking the true potential of memelements.

The first deliberate fabrication of a memelement only dates back 15 years to the physical realization of the memristor in 2008<sup>12</sup>. The massive technological potential of memristors soon became evident resulting in huge volumes of work dedicated to fabrication of memristors and their deployment in novel memory and computing hardware<sup>13–16</sup>. An understanding that the revolutionary potential of memelements is not limited to memristors but is also shared by its siblings—the memcapacitor and the meminductor- led to their physical realizations in 2019<sup>17</sup> and 2023<sup>18</sup> respectively. However, with work on physical memelements almost exclusively confined to memristors over the past 15 years, memcapacitors and meminductors remain largely unexplored despite being

Department of Electrical and Computer Engineering, Texas A&M University, College Station, TX 77840, USA.  
✉email: abhiram@tamu.edu; rusty.harris@tamu.edu

envisioned to possess superior energy efficiency owing to their inherent energy storage characteristics<sup>19</sup>. This work aims to bridge this gap by reporting a “locally active”<sup>20,21</sup> meminductor emulating second order neuronal behavior thus demonstrating “persistent dynamical behavior”.

A memelement passively coupled to a judiciously chosen passive network and driven by an appropriate DC excitation may yield persistent dynamical behavior only when biased at a “locally active (LA)” steady state<sup>22,23</sup>. The range of possible dynamical behaviors is in turn determined by the “order of complexity” of the memelement (number of coupled state variables) and thus, depends on device configuration<sup>24</sup>. Higher degrees of complexity yield more complicated dynamics. Since complex electrical responses in seemingly simple elements are commonplace in biological systems, designs of LA memelements derive inspiration from, and are aimed at emulating, biological brains thus constituting neuromorphic hardware architectures<sup>25–31</sup>.

While LA is understood to be the cause of such complexity, search for LA in a memelement is not trivial and is currently lacking a universal framework<sup>32</sup>. To address this problem, the “color map” approach has been developed in recent works exploring complexity in memristors to identify bias conditions that enable inversion of fluctuations and thereby, LA<sup>33,34</sup>. This technique is expanded to meminductors in our work and is used to investigate an uncoupled volatile meminductor for LA. In this paper, Sect. “[Meminductor and local activity principle](#)” is devoted to the fabrication of an uncoupled meminductor and investigation of its mathematical model for LA steady states using the color map approach. Section [Persistent dynamics in a passively coupled EOC meminductor](#) is dedicated to passively coupling the LA meminductor to a passive network to generate persistent dynamics and neuronal behaviors.

## Meminductor and local activity principle

### Introduction to a meminductor

A current ( $i(t)$ ) sourced inductor whose instantaneous inductance ‘ $L_{inst}$ ’ depends on an internal state variable  $s(t)$  constitutes a meminductor<sup>35</sup>. Mathematically, this dependence is described by  $L_{inst}=f_1(s(t))$ , where  $ds/dt=f_2(s, i)$ . As shown in Fig. 1a, the constitutive relationship of a meminductor relates the input current  $i(t)$  to the output flux  $\phi(t)$  as  $\phi(t)=L_{inst} \cdot i(t)$ . For a periodic, bipolar current excitation with zero mean, the state-dependent inductance results in the meminductor’s characteristic “pinched hysteresis” response in the  $\phi$  vs.  $i$  plane as shown in the cartoon in Fig. 1b<sup>36</sup>.

Unlike a nonlinear inductor, the instantaneous inductance  $L(t)$  of a meminductor is multivalued in current  $i(t)$  due to its dependence on  $s(t)$ . Hence, the phase difference between  $i(t)$  and  $L(t)$  is non-zero. This phase difference for an ideal meminductor is  $\pi/2$ , meaning that the instantaneous inductance monotonically decreases or increases as long as the polarity of the sourced current remains unchanged. This property was exploited in our recent report on the physical realization of the first deliberate meminductor<sup>18</sup> by facilitating the interaction of

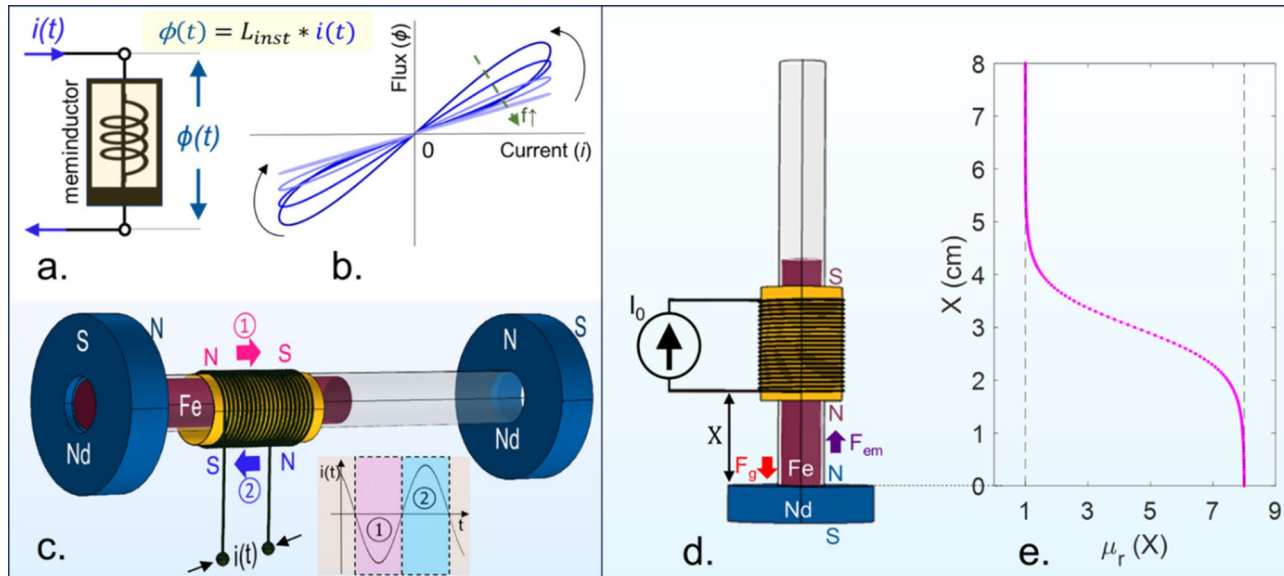


**Fig. 1.** Meminductor- introduction. (a) Symbol of a meminductor shown along with its constitutive state variables current ( $i$ ) and flux ( $\phi$ ). (b) Characteristic pinched hysteresis curve of the meminductor in the  $\phi$  vs.  $i$  plane. (c) Setup reported by the authors of this work in a previous publication on the physical realization of a continuum-memory meminductor. Magnetic poles on the winding are so set up that the winding moves to the right (left) during the negative (positive) half-cycle of input current thus monotonically decreasing (increasing) the inductance of the winding. (d) A volatile meminductor design employing a vertically oriented winding interacting with a neodymium permanent magnet. The winding moves under the influence of mutually opposing electromagnetic and gravitational forces. A ferromagnetic bar partially fills the core volume resulting in meminductance. (e) Relative magnetic permeability ( $\mu_r$ ) of the core volume of the winding modeled as a sigmoid function of its position,  $X$ .

two permanent magnets with an electromagnet as shown in Fig. 1c. State-dependence of inductance was realized by partially filling the electromagnet's core volume by a ferromagnetic bar, resulting in a position-dependent inductance. This setup results in a nonvolatile meminductor with the position of the winding relative to the ferromagnetic core being the internal state variable influencing the inductance. Since every position of the winding along the length of the core constitutes a nonvolatile state, volatile steady states are nonexistent and the meminductor realized in this previous work was hence described as a “continuum-memory meminductor”<sup>37</sup>.

However, as detailed later in Sect. Local activity in a meminductor, dynamical behavior may not emerge or persist in a passively coupled element unless it consists of volatile steady states<sup>38</sup>. Since the continuum-memory meminductor setup from our previous report consists exclusively of nonvolatile states, it is incapable of local activity. In this work, volatile steady states are induced by changing the horizontal orientation of the winding into a vertical orientation as shown in Fig. 1d such that the uncoupled meminductor is simultaneously influenced not only by an electromagnetic force but also a restorative gravitational force. The setup is so designed that a DC current sourced through the vertically oriented winding sets up magnetic poles on the winding which interact with a permanent magnet placed at the bottom to result in an upward force on the winding. The lower portion of the winding's core volume is filled with a ferromagnetic material such that the inductance of the winding decreases as its position is raised. The system therefore has a state-dependent inductance, where the state variable is the position of the winding relative to the permanent magnet. The position-dependent relative permeability of the core can be modeled as a sigmoid function as shown in Fig. 1e. For every value of sourced DC current ' $I$ ', there exists an equilibrium point at a height 'X' above the permanent magnet where the upward electromagnetic force and downward gravitational force balance each other. Once this current is withdrawn, the winding always returns to the bottom thus always converging onto the same steady state values of the state variable (position,  $X=0$ ) and inductance. Hence, gravitational force acts as a restoring force that lends volatility to the meminductor. A detailed explanation of the emergence of meminductive fingerprints in such configurations and challenges involving experimental extraction of the hallmark pinched hysteresis curve in parasitic resistance dominated setups has been provided in our previous report<sup>18</sup> and also included in the Supplementary Information section of this paper.

### Local activity in a meminductor

Local activity (LA) and local passivity (LP) of a meminductor respectively refer to the element's ability and inability to invert or amplify small fluctuations when biased at a steady state. Each steady state is also characterized by its stability: locally stable (LS) steady states attract neighboring trajectories while locally unstable (LU) steady states, repel. Together, LS vs. LU and LP vs. LA can provide a lot of insight into the network level dynamical behavior of a meminductor as described in this Sect<sup>39</sup>.

Consider a current-driven meminductor biased at the steady state  $(I, \Phi, X)$  where input current fluctuations  $\delta i(t)$  result in state variable fluctuations  $\delta x(t)$  and output flux fluctuations  $\delta \phi(t)$ . This meminductor is assured to be locally passive if the fluctuation energy  $\delta \epsilon$  is positive-definite for every  $t' > 0$  and  $\delta i(t) = \delta \phi(0) = \delta x(0) = 0$ <sup>40,41</sup>.

$$\delta \epsilon(t') \triangleq \int_0^{t'} \delta v(t) \times \delta i(t) dt \geq 0 \iff LP \quad (1)$$

This definition is mathematically rigorous and intuitively conveys the ability of an LA meminductor to invert fluctuations ( $\delta \epsilon < 0$ ) but is not experimentally convenient. Hence, Leon Chua developed an equivalent quantitative set of conditions to test for LP, which can be adapted for a meminductor as follows<sup>42,43</sup>. An uncoupled meminductor with a locally linearized transfer function  $\zeta(s) \triangleq \hat{\phi}(s)/\hat{i}(s)$ —where  $\hat{i}(s)$  and  $\hat{\phi}(s)$  denote the Laplace transforms of  $\delta i(t)$  and  $\delta \phi(t)$  respectively—is LA if any one of the two following mutually exclusive conditions holds:

- (A)  $\zeta(s)$  has a pole of any order in the closed right half plane (closed RHP:  $Rs \geq 0$ ) with the additional requirement that any simple poles on the imaginary axis have a non-positive-real (non-PR) residue **or**.
- (B)  $\zeta(s)$  has all its poles in the open left half plane (open LHP:  $Rs < 0$ ) and maps at least some points on the imaginary axis ( $Rs = 0$ ), i.e., “pure sinusoids”, into the open left half plane (open LHP:  $Rs < 0$ ).

where  $Rs$  is the real part of the complex angular frequency  $s$ . Condition (A) applies to LU systems since the presence of at least one pole in the closed RHP characterizes instability. Similarly, condition (B) applies to LS systems.

LU/LS and LP/LA are independent properties thus leading to four combinations: LU&LP, LU&LA, LS&LP, and LS&LA. Among these, LU&LP systems are characterized by simple poles on the imaginary axis with positive-real (PR) residue and are non-physical. Hence, any physically realizable LU system (poles in the closed RHP) is also LA, i.e., LU  $\Rightarrow$  LA, and such systems belong to the LU&LA class. This idea is captured in condition (A). On the other hand, condition (B) explains that not all LA systems are LU, i.e., LA  $\not\Rightarrow$  LU, and that there can exist LS&LA meminductors. LA may emerge in an LS meminductor (poles in open LHP) if  $\zeta(s)$  can map some pure sinusoids (i.e., some points on the imaginary axis) into the open LHP ( $Rs < 0$ ) where every point is characterized by a phase between  $\pi/2$  and  $3\pi/2$ . Since the output phase is closer to  $\pi$  than to 0 or  $2\pi$ , the phase-shifted sinusoids are qualitatively closer to inverted versions of the original sinusoids than to their non-inverted versions. Thus, condition (B) captures the ability of an LS&LA meminductor to invert fluctuations at certain “real” frequencies and systems satisfying this condition are said to be biased at the “Edge of Chaos” (EOC)<sup>44</sup>. Conversely, condition (A) is written as LA\EOC (read as LA but not EOC) and such behavior is called strict or unstable LA<sup>34</sup>.

For the emergence of dynamical patterns in physically realizable systems, LP systems are not of practical interest since Chua's "no-complexity theorem" proves that any input fluctuations in networks composed exclusively of LP systems are damped. For the fluctuations to instead be inverted/amplified, LA is a necessary requirement and thus leads to the expression, "Local activity is the origin of complexity."<sup>42</sup> Further, LA may only manifest in volatile steady states<sup>38</sup> thus necessitating the design of a volatile meminductor as described in Sect. [Introduction to a meminductor](#).

### Small signal model of an uncoupled volatile meminductor

The flux of the meminductor shown in Fig. [1d](#) can be expressed in terms of its state (position 'x') dependent inductance 'L' as

$$\varphi = L(x) i \quad (2)$$

where the state-dependent inductance  $L$  can be rewritten in terms of the state-dependent relative permeability  $\mu_r$  and a scaling factor 'c' as

$$L(x) = c \mu_r(x). \quad (3)$$

For a winding with  $N$  turns, cross-sectional area  $A$ , and length  $l$ , the scaling factor 'c' is given by

$$c = \frac{N^2 A}{l}. \quad (4)$$

On the other hand, the position-dependent relative permeability of the core can be modeled as a sigmoid function as shown in (5) where the parameter values have been chosen as  $\mu_{\max} = 8$ ,  $\alpha = 250 \text{ m}^{-1}$ , and  $\delta = 0.03 \text{ m}$  to replicate experimental results.

$$\mu_r(x) = \mu_{\max} - \frac{\mu_{\max} - 1}{1 + \exp(-\alpha(x - \delta))}. \quad (5)$$

A second order differential equation for the state variable 'x' can be developed using Newton's laws of motion by balancing the total upward and downward forces as

$$\frac{d^2x}{dt^2} = \frac{1}{m_T} (F_{\text{em}} - F_a - F_g) \quad (6)$$

where  $m_T$  is the total mass of the winding, and  $F_{\text{em}}$ ,  $F_a$ , and  $F_g$  respectively denote the electromagnetic, drag, and gravitational forces.

The electromagnetic force  $F_{\text{em}}$  can be approximated as<sup>45</sup>

$$F_{\text{em}} = \frac{3\mu_0\mu_r}{4\pi} \mathcal{M}_{\text{dPM}} \mathcal{M}_{\text{dwinding}} \left( \frac{1}{x^4} \right) \quad (7)$$

where  $\mathcal{M}_{\text{dPM}}$ ,  $\mathcal{M}_{\text{dwinding}}$  are the magnetic dipole moments of the permanent magnet and the winding respectively, and

$$\mathcal{M}_{\text{dwinding}} = N A i_w \quad (8)$$

where  $i_w$  is the winding current.

Hence,

$$F_{\text{em}} = K_1 \mu_r(x) \left( \frac{i}{x^4} \right) \quad (9)$$

where

$$K_1 = \frac{3\mu_0}{4\pi} \mathcal{M}_{\text{dPM}} N A. \quad (10)$$

Under the reasonable assumption that the winding moves slowly enough for the drag force  $F_a$  to be linearly proportional to the velocity of the winding,  $F_a$  can be expressed as

$$F_a = k_a \frac{dx}{dt} \quad (11)$$

where ' $k_a$ ' is the air drag coefficient.

The gravitational force  $F_g$  acting on the winding can be calculated as

$$F_g = m_T g \quad (12)$$

where 'g' is the acceleration due to gravity. Hence, (6) can be rewritten as

$$\frac{d^2x}{dt^2} = \frac{K_1}{m_T} \mu_r(x) \left( \frac{i}{x^4} \right) - \frac{k_a}{m_T} \frac{dx}{dt} - g. \quad (13)$$

Based on the experimental setup and resulting calculations, the following parameter values have been used in generating results reported in this publication:  $m_T = 2.6 \times 10^{-3}$  kg,  $K_1 = 7.6 \times 10^{-6}$  kg m<sup>5</sup> s<sup>-2</sup> A<sup>-1</sup>,  $k_a = 0.008$  kg s<sup>-1</sup>, and  $g = 9.8$  m s<sup>-2</sup>.

At a steady state ( $I, \Phi, X$ ), all the time derivatives reduce to zero. Hence, (14) gives the equilibrium condition

$$\frac{K_1}{m_T} \mu \frac{I}{X^4} = g \quad (14)$$

where,

$$\mu \triangleq \mu_r(x) |_{x=X}. \quad (15)$$

Investigating this setup for any possibility of EOC operation using Chua's quantitative conditions from Sect. [Local activity in a meminductor](#) requires linearizing this nonlinear model about the steady state ( $I, \Phi, X$ ) and evaluating the local dynamical response of the system to fluctuations of the input, output, and state variables. This can be done by considering fluctuations of  $i, \phi$ , and  $x$  about ( $I, \Phi, X$ )- respectively denoted as  $\delta i, \delta\phi$ , and  $\delta x$  (where  $(\delta i(t), \delta\phi(t), \delta x(t)) \triangleq ((i(t)-I), (\phi(t)-\Phi), (x(t)-X))$ - and evaluating their time evolution. From (2) and (3),

$$\frac{1}{c} \delta \varphi = \mu_r(x) |_{x=X} \delta i + I \delta \mu_r(x) \quad (16)$$

$$\Rightarrow \frac{1}{c} \delta \varphi = \mu_r(x) |_{x=X} \delta i + I \left( \frac{d}{dx} \mu_r(x) |_{x=X} \delta x \right). \quad (17)$$

From (15),

$$\frac{1}{c} \delta \varphi = \mu \delta i + I \mu' \delta x \quad (18)$$

where,

$$\mu' \triangleq \frac{d}{dx} \mu_r(x) |_{x=X}. \quad (19)$$

Similarly, from (13)

$$\frac{d^2(\delta x)}{dt^2} + \frac{k_a}{m_T} \frac{d(\delta x)}{dt} = \left( \frac{K_1}{m_T} \frac{\mu}{X^4} \right) \delta i + \left( \frac{K_1 I}{m_T} \left( \frac{\mu'}{X^4} - \frac{4\mu}{X^5} \right) \right) \delta x. \quad (20)$$

Meminductance in a winding originates from a non-zero phase difference between the input current and the state variable (i.e., position). Fluctuations in current therefore lead to phase-shifted fluctuations in position which in turn contribute to phase-shifted fluctuations in flux. Hence, according to (20), the total fluctuations in output flux have two components: an in-phase primary component from current fluctuations and a phase-shifted secondary component from phase-shifted position fluctuations. These phase-shifted secondary fluctuations hold the key to inverting the initial fluctuations and thereby, to lending LA to the element.

With the Laplace transforms of the fluctuations  $(\delta i(t), \delta\varphi(t), \delta x(t))$  respectively denoted by  $(\hat{i}(s), \hat{\varphi}(s), \hat{x}(s))$ , and the reasonable assumption that the initial conditions of the fluctuations are all zero, Laplace transforms of (18) and (20) respectively yield (21) and (22).

$$\frac{1}{c} \hat{\varphi} = \mu \hat{i} + \mu' I \hat{x} \quad (21)$$

$$\hat{x} = \frac{\left( \frac{K_1}{m_T} \frac{\mu}{X^4} \right) \hat{i}}{s^2 + \frac{k_a}{m_T} s - \left( \frac{K_1 I}{m_T} \left( \frac{\mu'}{X^4} - \frac{4\mu}{X^5} \right) \right)}. \quad (22)$$

Eliminating  $\hat{x}(s)$ ,

$$\frac{\hat{\varphi}}{\hat{i}} = c\mu + c\mu' \left( \frac{K_1 I}{m_T} \frac{\mu}{X^4} \right) \frac{1}{s^2 + \frac{k_a}{m_T} s - \left( \frac{K_1 I}{m_T} \left( \frac{\mu'}{X^4} - \frac{4\mu}{X^5} \right) \right)}. \quad (23)$$

Combining this result with the equilibrium condition from (14) yields the small signal transfer function

$$\zeta(s) \triangleq \frac{\hat{\varphi}}{\hat{i}} = c\mu \frac{s^2 + \frac{k_a}{m_T} s + \frac{4g}{X}}{s^2 + \frac{k_a}{m_T} s - g \left( \frac{\mu'}{\mu} - \frac{4}{X} \right)}. \quad (24)$$

### EOC bias conditions in an uncoupled volatile meminductor

As described in Sect. [Local activity in a meminductor](#), EOC bias conditions of a vertically oriented, DC current driven meminductor with a superimposed current fluctuation ( $\delta i$ ) as shown in Fig. [2a](#) may be investigated based on the locations of the poles and zeros of its linearized transfer function on the  $s$ -plane. The second order transfer function  $\zeta(s)$  from (24) has a complex conjugate pair of zeros located at

$$s_z = -\frac{k_a}{2m_T} \pm \frac{1}{2} \sqrt{\left(\frac{k_a}{m_T}\right)^2 - \frac{16g}{X}}. \quad (25)$$

and a complex conjugate pair of poles located at

$$s_p = -\frac{k_a}{2m_T} \pm \frac{1}{2} \sqrt{\left(\frac{k_a}{m_T}\right)^2 - \frac{16g}{X} + 4g\frac{\mu'}{\mu}}. \quad (26)$$

One pole-zero pair,  $(s_{p1}, s_{z1})$ , resides above the real axis and the other,  $(s_{p2}, s_{z2})$ , below. Since  $X$  is always positive, the real part of  $s_z$  is always negative. On the other hand, for  $\mu_r$  modeled as a sigmoid as shown in Fig. [2b](#),  $\mu$  is always positive while  $\mu'$  is always non-positive, thus resulting in the real part of  $s_p$  also being always negative. Since the real parts of both poles are negative, the system is always LS. Hence, any LA may only result from biasing the meminductor in the EOC regime. Such bias conditions may be evaluated by studying the system's

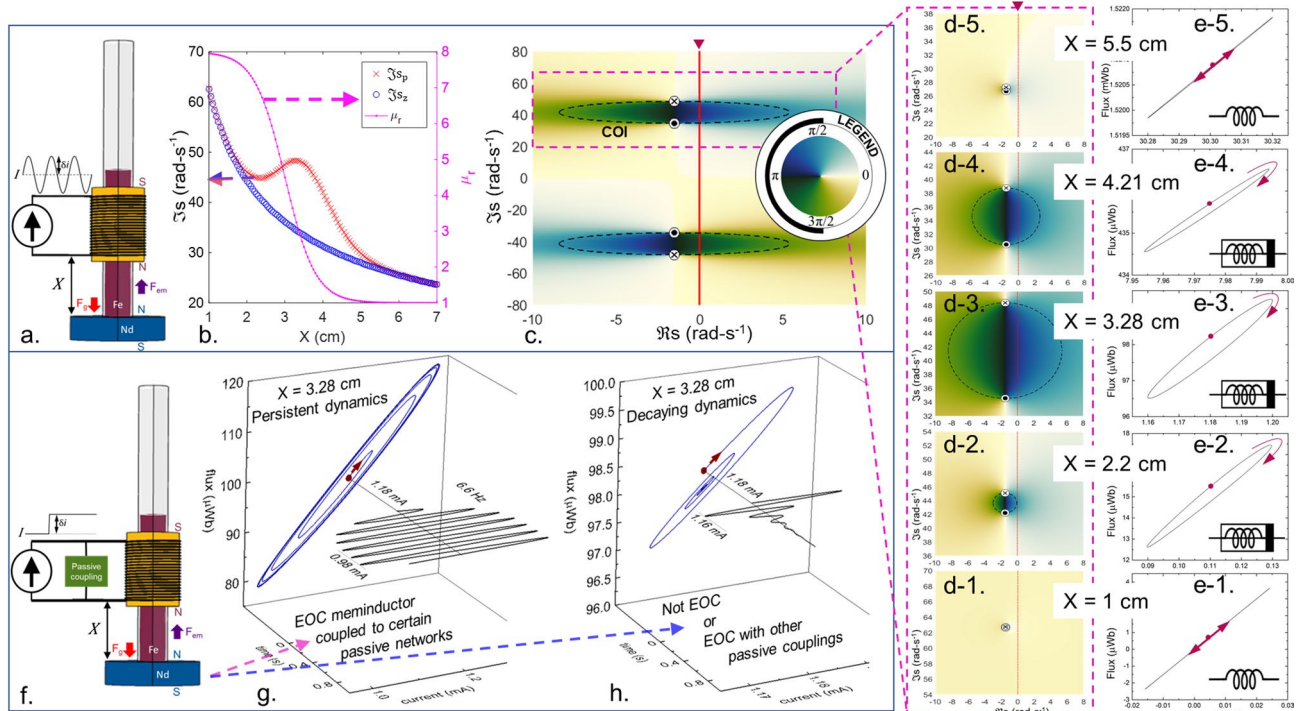


**Fig. 2.** EOC bias conditions in an uncoupled volatile meminductor. **(a)** A volatile meminductor driven by a DC current  $I$  with a small sinusoidal current of peak amplitude  $\delta i$  superimposed. **(b)** Imaginary parts of the pole-zero pair located above the real axis, and relative permeability ( $\mu_r$ ) of the winding core shown as functions of the state variable,  $X$ . Transition region in the  $\mu_r$  profile coincides with a separation of the pole and zero. **(c)** Pole-zero separation results in a Contour of Inversion (COI) in the complex  $s$ -plane. Color of each point represents the output phase of that point when transformed by the transfer function  $\zeta(s)$  according to the colormap legend shown in the inset. Complex conjugate pole-zero pairs result in two contours of inversion symmetric about the real axis. Result shown for  $X = 3.28$  cm. **(d)** Locations of the pole and zero (for the pole-zero pair above the real axis) in the complex  $s$ -plane for different values of the state variable,  $X$ .  $X = 1$  cm results in negligible pole-zero separation (**d-1**), while  $X = 2.2$  cm shows a more pronounced separation resulting in a COI (**d-2**). Further increase in  $X$  results in the COI crossing the imaginary axis, thereby resulting in EOC. Size of COI increases with position until  $X = 3.28$  cm (**d-3**) and then decreases, as shown for  $X = 4.21$  cm (**d-4**) finally becoming negligible, shown for  $X = 5.5$  cm (**d-5**). **(e)** Small signal flux vs. current response shown for  $X = 1$  cm (**e-1**),  $X = 2.2$  cm (**e-2**),  $X = 3.28$  cm (**e-3**),  $X = 4.21$  cm (**e-4**), and  $X = 5.5$  cm (**e-5**). **(f-h)** A locally stable volatile meminductor driven by a DC current  $I$  with a small step fluctuation of amplitude  $\delta i$  superimposed. When coupled to an external passive network, an EOC meminductor may result in persistent dynamics for certain couplings (**g**) and in decaying dynamics for other couplings (**h**). A meminductor not biased at the EOC always results in decaying dynamics.

ability to invert fluctuations. Also, since  $\left(\frac{k_a}{m_T}\right)^2 \ll \frac{16g}{X}$  in the setup considered, the real parts of poles and zeros coincide for all practically relevant steady states. However, the imaginary parts of each pole-zero pair do not necessarily coincide as shown in Fig. 2b.

The imaginary parts of  $s_{p1}$  and  $s_{z1}$  are shown along with  $\mu_r$  in Fig. 2b as functions of the winding's position  $X$ . Since  $\mu$  can be considered practically constant for winding positions  $X < 1$  cm and  $X > 6.5$  cm,  $\mu' \approx 0$ , and the poles and zeros of  $\zeta(s)$  annihilate each other resulting in a constant transfer function. However, for  $1 \text{ cm} < X < 6.5 \text{ cm}$ , the small signal permeability is no longer constant and hence,  $\mu' \neq 0$ , resulting in the pole-zero pairs separating from each other. In particular, from Fig. 2b, while the zero continues to move towards the real axis as  $X$  increases, the pole goes against the initial trend of moving towards the real axis and instead, briefly moves farther away. This results in an increasing pole-zero separation which peaks at  $X = 3.28$  cm. The pole then returns to the original trend of moving towards the real axis with increasing  $X$ , thus gradually lowering the pole-zero separation and finally colliding with the zero around  $X = 6.5$  cm.

In search for potential EOC bias conditions, it is of interest to track the phase shift induced by  $\zeta(s)$  on each point on the complex  $s$ -plane for different winding positions, i.e.,  $X$ . This can be visualized for each complex coordinate  $s = x + iy$  by evaluating its output phase  $\angle\zeta(s)$  and representing this phase by the color of the corresponding point on the  $s$ -plane<sup>33</sup>. The colormap<sup>46,47</sup> used in this work is shown in the inset of Fig. 2c and poles and zeros are indicated by the symbols  $\otimes$  and  $\odot$  respectively. Figure 2c illustrates the two pole-zero pairs for  $X = 3.28$  cm, with both pairs located in the open LHP and one pair each located above and below the real axis as previously described. Pole-zero separation leads to the emergence of a “Contour of Inversion” (COI) - shown as a black dashed circle- and for the setup being investigated, the emerging contour is a circle with the pole and the zero of each pole-zero pair as its diametric ends. The area enclosed by the COI is the collection of all points on the  $s$ -plane which have output phases between  $\pi/2$  and  $3\pi/2$ . Points along the diameter joining the pole and zero correspond to an output phase of  $\pi$ , and the line is hence termed the “Line of Inversion” (LOI). Figure 2d-1 through 2(d-5) show the pole-zero separation and COI for different values of  $X$ .

As described in Sect. [Local activity in a meminductor](#), an LS meminductor is said to be biased at the edge of chaos if there exist some points on the imaginary axis which are mapped by  $\zeta(s)$  into the open LHP, i.e., with output phase in the range  $(\pi/2, 3\pi/2)$ . Hence, the meminductor setup modeled here is EOC only for those values of  $X$  for which the COI intersects the imaginary axis at least once. Therefore, while the absence of a COI eliminates the possibility of EOC biasing (see Fig. 2d-1, d-5), the existence of COI alone does not guarantee EOC as shown for  $X = 2.2$  cm (see Fig. 2d-2) but instead needs the COI to cross the imaginary axis as shown for  $X = 3.28$  cm (see Fig. 2d-3) and  $X = 4.21$  cm (see Fig. 2d-4). Overall, the COI crosses the imaginary axis in the range  $2.21 \text{ cm} < X < 5.08 \text{ cm}$  thus encompassing the range of  $X$  where the meminductor is biased at the edge-of-chaos. Any value of  $X$  outside this range results in a locally passive meminductor.

The emergence of a COI in the range  $1 \text{ cm} < X < 6.5 \text{ cm}$  is a consequence of the element locally demonstrating a state-dependent inductance (i.e.,  $\mu' \neq 0$ ) thus yielding a meminductor. Its response to a small sinusoidal current  $\delta i$  (chosen as  $20 \mu\text{A}_{\text{peak}}$  for illustration) superimposed on the DC current  $I$  is a multi-valued hysteretic lobe in the flux-current plane as shown in Fig. 2e-2, e-3, e-4. COI vanishing on either side of this range correlates with the permeability in a small signal model being a constant (i.e.,  $\mu' \approx 0$ ) and the resulting state-independent inductance thus locally yielding a linear inductor. The flux vs current response of this linear inductor to a small sinusoidal current excitation about the DC current tends towards single-valued behavior as shown in Fig. 2e-1, e-5.

Points on the imaginary axis correspond to pure sinusoids, with the imaginary parts of the points representing the sinusoids' respective angular frequencies ' $\omega$ '. At  $X = 3.28$  cm, since the COI is the largest, the widest range of fluctuations can result in EOC, with the frequencies of such fluctuations ranging between  $35 \text{ rad}\cdot\text{s}^{-1}$  (i.e.,  $5.57 \text{ Hz}$ ) and  $48 \text{ rad}\cdot\text{s}^{-1}$  (i.e.,  $7.64 \text{ Hz}$ ). The lowest and highest frequencies that can result in EOC turn out to be  $30.3 \text{ rad}\cdot\text{s}^{-1}$  (i.e.,  $4.82 \text{ Hz}$ ) and  $48 \text{ rad}\cdot\text{s}^{-1}$  (i.e.,  $7.64 \text{ Hz}$ ), respectively.

A passively coupled EOC biased meminductor as shown in Fig. 2f may result in either persistent dynamics or decaying dynamics depending on the passive network coupled to it. These cases at  $X = 3.28$  cm are illustrated with cartoons in Fig. 2g, h respectively, with the amplified fluctuations in Fig. 2g shown to arbitrarily converge onto a stable oscillation with an amplitude of  $0.2 \text{ mA}_{\text{peak}}$  for illustrative convenience. In a real setup, the oscillation amplitude depends on several factors including the properties of the coupling network, and depending on the order of complexity, persistent dynamics may manifest not just as periodic oscillations but also as other dynamical responses such as periodic bursts and chaotic oscillations. Designing a network of passive components which, when coupled to the volatile meminductor fabricated, yields persistent dynamics in a real-world experimental setup forms the bulk of Sect. [Persistent dynamics in a passively coupled EOC meminductor](#).

It is useful to note two special cases of the EOC meminductor setup. The first is an ideal, non-physical scenario of zero air resistance, i.e.,  $k_a = 0$ . In this case, both poles of the system land on the imaginary axis (simple poles with non-positive-real residue) thereby making the meminductor LA\EOC, i.e., the hypothetical system would be locally active for all steady states and results in persistent dynamics even when uncoupled. The second case is of replacing the meminductor by a nonlinear inductor, which may be theoretically achieved via a hypothetical inductor whose instantaneous inductance depends only on the instantaneous current flowing through the winding (i.e.,  $\varphi = L(i) \times i$ ). In this case, following the same linearization procedure results in a constant transfer function for  $\zeta(s)$  which physically corresponds to fluctuations resulting in transient decaying dynamics regardless of the choice of passive coupling. This result hence reiterates the necessity of components with state-dependent electrical properties, i.e., mem-elements, for the possibility of EOC and any ensuing complexity.

### EOC bias with positive differential inductance (PDL)

Noting that flux refers to the time integral of voltage in the generalized context of nonlinear electronics,  $\frac{\hat{\varphi}}{i}$  may be rewritten as  $\frac{\hat{v}}{s}$ , where  $v(t)$  is the voltage across the winding. Identifying that  $\frac{\hat{v}}{i}$  is the small signal impedance “Z” of the winding,

$$\zeta(s) = \frac{1}{s} Z(s). \quad (27)$$

Since multiplication by  $1/s$  in the Laplace domain translates to integration in the time domain,  $\zeta$  is hereafter given the name “Impedance momentum” conforming to the norm of calling electrical variables like charge and flux (i.e., time integrals of current and voltage, respectively), current momentum and voltage momentum, respectively<sup>48</sup>.

The volatile meminductor modeled here has been shown to have a complex conjugate pair of poles (and zeros) and hence constitutes a “2-D mem-system”. This contrasts with one-pole-one-zero mem-systems, e.g., 1-D electrothermal memristors, where the singular pole and zero of the impedance transfer function must both be purely real with the pole in the open LHP and the zero in the open RHP for EOC operation<sup>38,49</sup>. Since the pole and zero flip for the admittance transfer function ( $Y \triangleq 1/Z$ ),  $Y(s)$  has its pole in the RHP and hence cannot result in EOC. Thus, the set of usable source variables is restricted to current in 1-D electrothermal memristors. Hence, LA steady states may only be accessed by sourcing current but not voltage. This restriction mathematically corresponds to voltage being a “well-defined” function of current but current being multi-valued in voltage thus resulting in a negative differential resistance (NDR) region on the DC  $V$ - $I$  curve<sup>50,51</sup>.

However, in the case of two-pole-two-zero systems with real parts of *all* poles and zeros negative (like the meminductive setup described here), the transfer functions for both impedance momentum ( $\zeta$ ) and its inverse ( $\zeta^{-1}$ ) may potentially result in the EOC regime since interchanging the poles and zeros would still place *all* the poles in the open LHP. Hence, neither current nor flux may be ruled out from the set of source variables that can bias the system in EOC. This implies that the meminductor *must* be well-defined in both current and flux (i.e., both variables must be single-valued functions of each other) and hence, *must* demonstrate positive differential inductance (PDL) in the entirety of its DC  $\Phi$ - $I$  curve. To verify this requirement in the current setup, rewrite the steady state Eq. (14) to yield

$$\mu = g \frac{m_T X^4}{K_1 I}. \quad (28)$$

Combining (28) with the steady state flux equation  $\Phi = c\mu I$ ,

$$\Phi = c g \frac{m_T}{K_1} X^4. \quad (29)$$

The differential inductance,  $d\Phi/dI$  can be calculated by differentiating (29) with respect to  $I$  to give

$$\frac{d\Phi}{dI} = 4 \frac{\Phi}{X} \frac{dX}{dI}. \quad (30)$$

Since  $\Phi$  and  $X$  are always positive in the experimental setup and  $dX/dI > 0$  (from (28)),  $d\Phi/dI$  is always positive, thus confirming Positive Differential Inductance (PDL) for all allowable steady states ( $I, \Phi, X$ ) as shown in Fig. 3a, b. Generalizing these findings to all memelements, these results confirm that a negative differential transfer

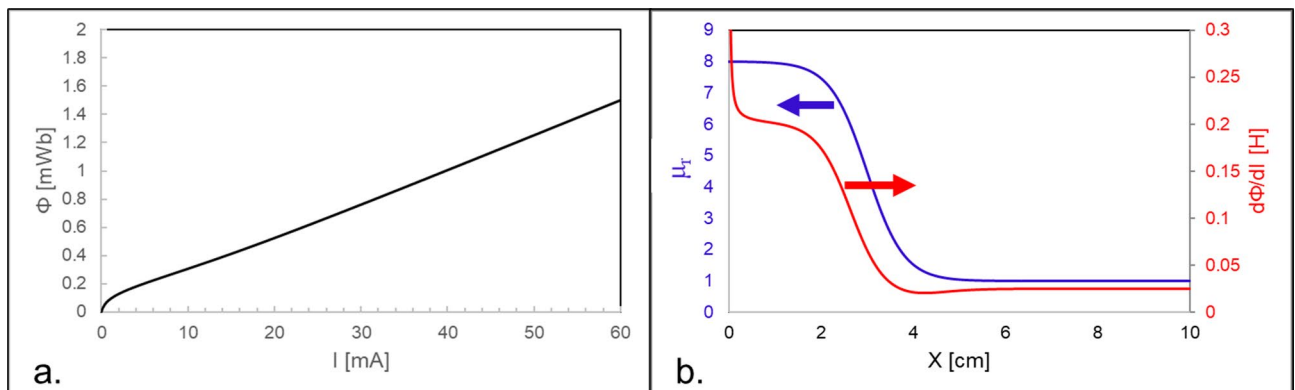


**Fig. 3.** EOC operation with exclusively positive differential inductance. (a) DC  $\Phi$ - $I$  curve of the meminductor. (b) Differential inductance shown as a function of the state variable  $X$ . Relative permeability  $\mu_r$  also superimposed for reference.

function (i.e., negative differential resistance in memristors, negative differential capacitance in memcapacitors, and negative differential inductance in meminductors) is not a prerequisite for edge-of-chaos operation and persistent dynamical behavior.

### Equivalent circuit model with pseudo-elements

At the circuit level, modeling a virtual equivalent circuit yielding the same functional form as the transfer function  $\zeta(s)$  is useful since any negative pseudo-elements in the equivalent circuit can hint towards locally active behavior and corroborate the results from Sect. [EOC bias conditions in an uncoupled volatile meminductor](#). The caveat here is that such negative pseudo-elements can only point to the presence of potential LA in the system described by  $\zeta(s)$  but can neither confirm it nor offer insights into its physical causes<sup>32</sup>. Also, such equivalent circuits are not unique and multiple such circuits can be conceived, all connected by the common feature that their transfer functions have the same functional form with at least one pseudo-element being negative.

Consider the transfer function  $\zeta_1(s)$  in (31), which is the same as  $\zeta(s)$  from (24), except with the scaling factor  $c\mu$  omitted for convenience.

$$\zeta_1(s) = 1 - \frac{r}{s^2 + ps + q + r}, \quad (31)$$

where,  $p \triangleq \frac{k_a}{m\tau}$ ,  $q \triangleq \frac{4g}{X}$ , and  $r \triangleq -g\frac{\mu'}{\mu}$ . Here,  $p$ ,  $q$ , and  $r$  end up being always non-negative since  $\mu'$  is non-positive and all other terms are strictly positive.

From (27), it can be easily shown that the impedance momentum for a linear inductor is  $L$ , for a linear resistor,  $R/s$ , and for a linear capacitor,  $1/Cs^2$ , where  $R$ ,  $L$ , and  $C$  are the resistance, inductance, and capacitance of the resistor, inductor, and capacitor, respectively. Hence, the impedance momentum transfer function for the virtual equivalent circuit shown in Fig. 4a is given by

$$\zeta(s) = 1 + \frac{\left(\frac{1}{C}\right)}{s^2 + s\left(\frac{1}{RC}\right) + \left(\frac{1}{LC}\right)}. \quad (32)$$

Comparing Eqs. (31) and (32),  $C = -1/r$ ,  $R = -r/p$ , and  $L = -r/(q+r)$ . As shown in Fig. 4b, since  $p$ ,  $q$ , and  $r$  are all non-negative,  $L$ ,  $C$ , and  $R$  are all non-positive, thus resulting in negative pseudo-elements and indicating potential LA in the system defined by (32). Also, it is to be noted that  $R$ ,  $L$ , and  $C$  reduce to short circuits outside the meminductive range, i.e., for  $X < 1$  cm or  $X > 6.5$  cm where  $\mu' = 0$ , thus reiterating the conclusion that LA cannot emerge if the inductance is locally state-independent. On the other hand, a negative pseudo-element- as found for  $1 \text{ cm} < X < 6.5 \text{ cm}$ - cannot directly point to LA, or by extension, EOC, but can only point to the existence of a COI (Contour of Inversion). For example, this can be seen for  $X = 2.2 \text{ cm}$  for which  $R$ ,  $L$ , and  $C$  are all negative, but the meminductor is not EOC since the COI does not cross the imaginary axis (recall Fig. 2d).

To summarize, the emergence of a hysteretic lobe in the flux vs. current plane, the emergence of a COI in the  $s$ -plane, and the presence of negative pseudo-elements in the small-signal equivalent LCR circuit are all equivalent conditions. Therefore, satisfying any one of these conditions guarantees the other two. Importantly, these conditions can only hint towards the possibility of EOC operation but cannot guarantee it.

### Persistent dynamics in a passively coupled EOC meminductor

#### Circuit design and realization

Achieving persistent oscillatory dynamics in an EOC-biased meminductor when connected to a network of passive circuit elements requires judicious choice of the LP coupling network. Motivated by Reenstra's low frequency oscillator circuit<sup>21,52</sup>, a current divider circuit as shown in Fig. 5a is identified as a candidate to realize a DC current driven, meminductor based, oscillator circuit, where the meminductor is connected in parallel with a passive component whose resistance  $R_p$  is designed to depend on the state variable of the meminductor (i.e.,

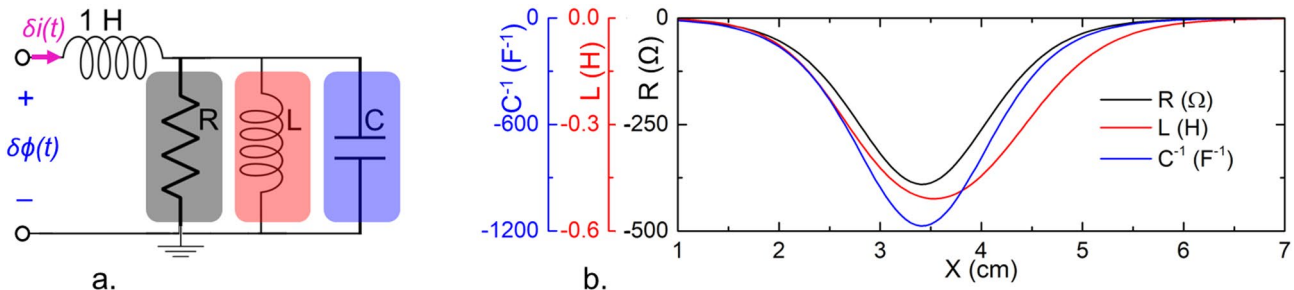


**Fig. 4.** Virtual equivalent linear circuit. (a) Linear RLC circuit yielding the same transfer function as the small-signal model of the uncoupled volatile meminductor. (b)  $R$ ,  $L$ , and  $C$  values extracted by comparing the transfer functions of the meminductor and the equivalent circuit plotted as functions of the state variable,  $X$ .  $R$ ,  $L$ , and  $C$  are all negative within the meminductive range and reduce to short-circuits outside.

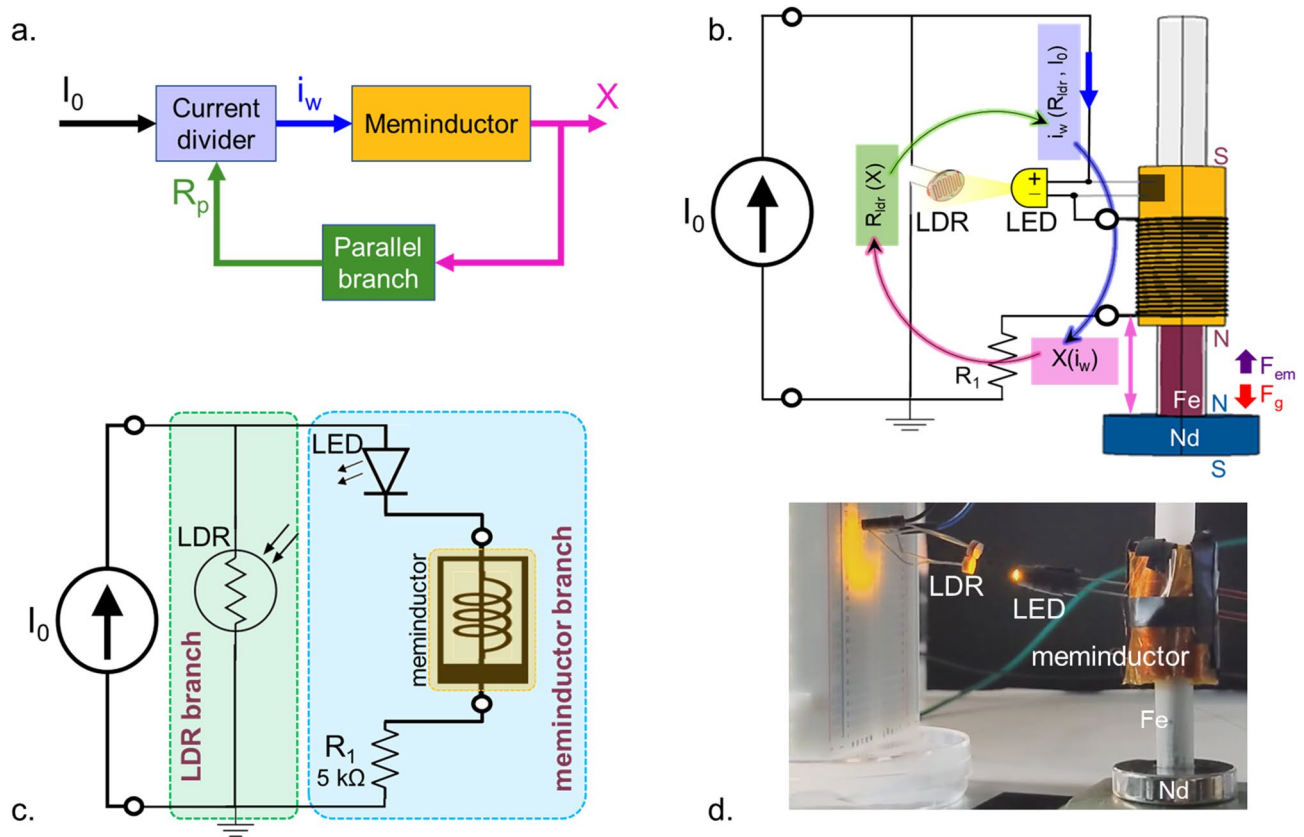


**Fig. 5.** Design of coupling network for persistent dynamics. (a, b) Design philosophy to setup a closed loop feedback mechanism shown as a block diagram (a) and as an electromechanical circuit (b). Meminductor branch current  $i_w$  influences the state variable  $X$  which in turn influences the resistance of the parallel branch  $R_p$ . Change in  $R_p$  results in a change in  $i_w$  thus repeating the cycle. The parallel branch is realized as a light-dependent-resistor (LDR), whose resistance depends on the position of an LED attached to the winding thus coupling  $R_p$  to  $X$ . (c) Electrical circuit representation of the setup. (d) Picture of experimental setup showing the LDR being illuminated by the LED attached to the winding.

$R_p(X)$ ). A variation in the meminductor branch current  $i_w$  results in a variation in  $X$  which in turn triggers a change in  $R_p$ . For a given source current  $I_0$ , a change in  $R_p$  in turn serves to alter both branch currents thus setting up a closed feedback loop and thereby, a potentially oscillatory mechanism. This design philosophy is shown in Fig. 5b and perpetual oscillatory behavior in this setup can be physically realized by careful choice of the parallel circuit constituents and the mechanism that couples  $X$  and  $R_p$ .

As shown in Fig. 5b, the parallel branch in this work comprises a light dependent resistor (LDR) whose resistance depends on the intensity of light illuminated on its surface. The meminductor branch has a yellow LED physically attached to, and electrically connected in series with, the winding. The LDR and LED are positioned such that the light from the LED illuminates the LDR only when the winding is raised by heights in the range  $2 \text{ cm} < X < 5 \text{ cm}$ . With shields to block off stray ambient light in place, the LDR has a “dark” resistance of over  $150 \text{ k}\Omega$  when not illuminated and “light” resistance as low as  $5 \text{ k}\Omega$  when illuminated by an LED driven by a current of  $30 \text{ mA}$  and placed  $3 \text{ cm}$  away. To increase the active surface area of the LDR, two LDRs have been connected in parallel, thus resulting in a minimum resistance of  $\sim 2.5 \text{ k}\Omega$ . The maximum inductance of the winding (i.e., at  $X=0$ ) is  $150 \text{ mH}$ . Hence, at frequencies below  $10 \text{ Hz}$ , its instantaneous inductive reactance  $X_L$  is less than  $10 \text{ }\Omega$  which is negligible in comparison with the series winding resistance of  $\sim 700 \text{ }\Omega$ . A  $5 \text{ k}\Omega$  power resistor is also connected in series in the meminductor branch, which along with the winding resistance and the LED resistance (roughly  $150 \text{ }\Omega$  and  $100 \text{ }\Omega$  for a yellow LED at  $10 \text{ mA}$  and  $25 \text{ mA}$ , respectively) brings the total resistance of the branch to about  $6 \text{ k}\Omega$ . The power resistor is only added to ensure that at least  $50\%$  of the sourced current flows through the LDR branch under maximum illumination when the LDR resistance reaches its minimum value of  $\sim 2.5 \text{ k}\Omega$ . The electrical circuit representation of the setup is shown in Fig. 5c and the experimental setup demonstrating the LED illuminating the LDR when the winding has been raised due to the meminductor branch current is shown in Fig. 5d.

## Results and discussion

Figure 6a shows the electrical circuit representation of the described setup with the resulting current divider circuits for the cases of maximum and minimum illumination of the LDR highlighted. When the winding is at the bottom, the LDR not being illuminated results in maximum LDR resistance ‘ $R_{LDR}$ ’ thus resulting in

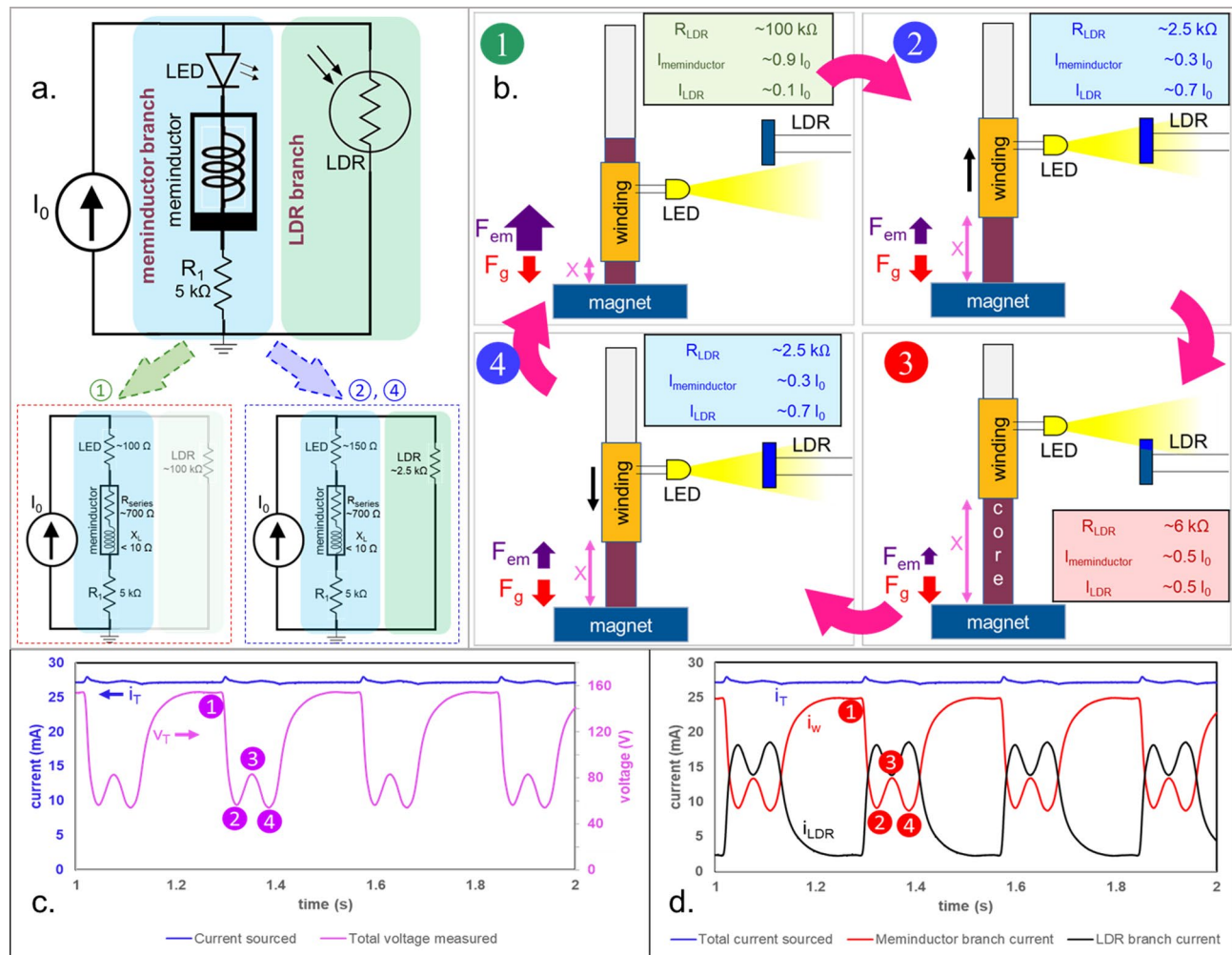


**Fig. 6.** Circuit setup and results. **(a)** Electrical circuit representation of the meminductor coupled to an LP network. The two border cases of no illumination and maximum illumination of the LDR highlighted in the insets. **(b)** Setup configuration shown for different timeslices during a single cycle, labelled ①–④. Instantaneous values of the LDR resistance and branch currents for each timeslice are shown in the inset of each panel. **(c)**, **(d)** Sourcing a constant current of 27 mA results in persistent oscillations due to a dynamically changing load. Oscillations in total voltage measured,  $V_T$  **(c)** and individual branch currents,  $i_w$  and  $i_{LDR}$  **(d)** shown, along with timeslice labels, ①–④.

maximum  $i_w$  and thereby, maximum voltage drop and upward electromagnetic force. If the electromagnetic force is strong enough to overcome limiting friction between the winding and the shaft along which it moves, the winding moves upward in search of an equilibrium point where the electromagnetic and gravitational forces balance each other out. For most configurations, the winding, aided by air drag and friction (both static and dynamic), succeeds in finding such a stable equilibrium point. However, when the meminductor is biased at the edge of chaos, it is possible to destabilize equilibrium points over a range of values of  $X$  by carefully adjusting parameters such as the horizontal and vertical distances between the LED and LDR. Such adjustment ensures that when the winding reaches the previously sought equilibrium point, the LDR being illuminated lowers  $R_{LDR}$  and thereby,  $i_w$ . Hence, the winding no longer has the required electromagnetic force to stay at that height since some of its current has been routed through the LDR branch. Therefore, the winding loses height due to gravity and in this process, the LDR illumination is lowered. Thus, the winding once again draws more current and thereby experiences an increased electromagnetic force. This process can repeat perpetually, thus resulting in persistent oscillations as depicted in Fig. 6b for different slices of time during an oscillation cycle.

For such a carefully arranged configuration as shown in Fig. 6b, as the winding moves from position ① to position ②, the light emitted by the LED gradually illuminates larger cross-sections of the LDR, thereby progressively lowering its resistance. Hence, the meminductor current  $i_w$  reaches its minimum at ②, which results in minimum voltage drop  $V_T$  as shown in Fig. 6c, d for  $I_0 = 27\text{ mA}$ . However, in spite of  $i_w$  being at a minimum, the winding does not stop its upward motion at ② due to inertia of motion often carrying the winding beyond ② to ③. In this part of the winding's journey, the LDR illumination gradually decreases thus resulting in a progressively higher LDR resistance. This translates to increasing  $i_w$  and  $V_T$  (see Fig. 6c, d). Once the upward

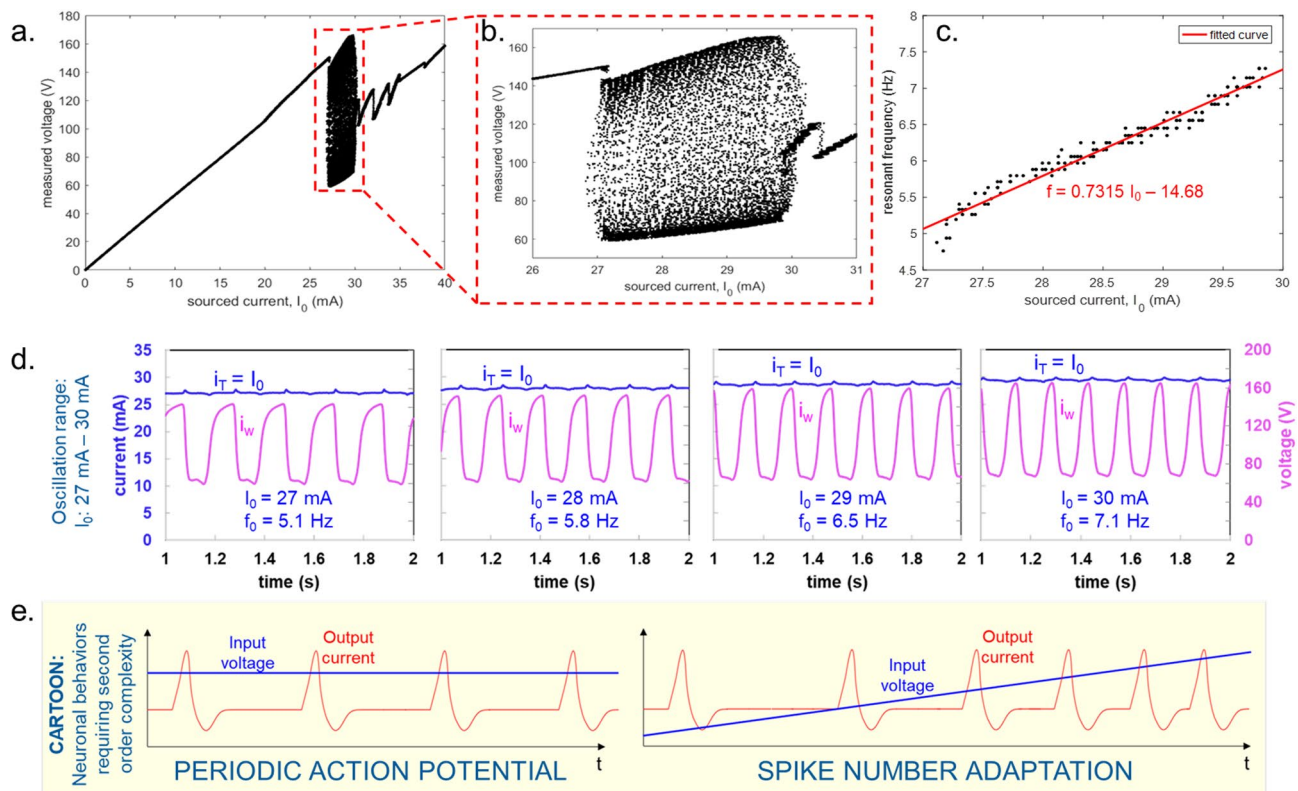


**Fig. 7.** Source-current dependent bifurcation. (a, b) Input currents  $I_0$  in the range 27 mA–30 mA destabilize steady states resulting in astable behavior and thereby, persistent oscillations. Steady states are stable on either side of this parametric range. Voltage oscillations in the astable region highlighted in (b). (c,d) Within the astable region, oscillation frequency increases as  $I_0$  increases. Frequency of oscillations as a function of  $I_0$  shown in (c) and time domain response for different values of  $I_0$  shown in (d). (e) Cartoons depicting second order neuronal properties, namely periodic action potential generation and spike number adaptation. Experimental results shown in (a–d) highlight the meminductor's ability to mimic such neuronal activity when appropriately coupled, thereby showing evidence of its potential in neuromorphic hardware development.

inertial motion stops, the winding begins to lose height and as it returns from ③ to ①, it once again crosses a point of maximum LDR illumination at ④ which is physically the same location as ②. Hence, as the winding moves from ③ to ④,  $i_w$  and  $V_T$  decrease to their respective minima, and as the winding continues from ④ to ①, they increase again.

It is important to note that achieving a persistent oscillatory response requires the winding to pass through the maximum LDR illumination position. This can be achieved through a current ramp (Supplementary Video-1) that forces the winding to approach the maximum LDR illumination position with upward velocity. If the winding is simply placed in the maximum LDR illumination position, then a local minimum in overall energy allows a stable position to be achieved. However, this state can be physically perturbed (Supplementary Video-3), also resulting in a persistent oscillatory state.

#### Source current dependent parametric bifurcation

In the described setup, oscillations emerge only when the meminductor is biased at the edge of chaos which requires the winding position to be in the range  $2.2 \text{ cm} < X < 4.75 \text{ cm}$  (see Sect. [EOC bias conditions in an uncoupled volatile meminductor](#)). Accounting for the static and dynamic friction components between the core shaft and the winding, these positions typically correspond to meminductor branch currents in the range  $15 \text{ mA} < i_w < 30 \text{ mA}$ . Hence, when the source current  $I_0$  results in values of  $i_w$  outside this range, oscillatory behavior is not possible. For source currents resulting in values of  $i_w$  within this desirable range, the very emergence of oscillations and the range of values of  $i_w$  which result in said oscillations are both sensitively dependent on the setup parameters (LED-LDR spacing and orientation etc.). Subtle changes in these parameters translate to considerable changes in the profile, frequency, and amplitude of oscillations, with persistent oscillations themselves often changing into decaying dynamics by a mere nudge of the LDR position (see Supplementary Video-2). On the other hand, when the setup is left undisturbed (experimentally tested for a duration of 2 h), the oscillations have been found to not stop until the source current was turned off.

Figure 7 demonstrates astable, oscillatory behavior with the setup configured to result in oscillations in the range  $27 \text{ mA} < I_0 < 30 \text{ mA}$ . As  $I_0$  is gradually increased from 0 in a quasi-DC sweep, the measured voltage increases linearly with the source current as long as the winding remains stationary at the bottom. In this regime,

since the system converges to a stable steady state for each  $I_0$ , a steady state voltage emerges once the transients die out. Plotting this steady state voltage as a function of  $I_0$  hence results in a single-valued curve in the source-current-dependent bifurcation plot as shown in Fig. 7a. However, once  $I_0$  reaches  $\sim 27$  mA, the electromagnetic force is strong enough to overcome the limiting friction between the core shaft and the winding, and the winding abruptly jumps up and starts oscillating. In this regime, since the steady states have been destabilized, the system cannot converge to a steady state and the bifurcation plot for each  $I_0$  hence shows not a single data point but a continuum of voltage points in the range 58–144 V as highlighted in Fig. 7b. As the current is further increased, the oscillations grow both in amplitude and frequency and thus, the oscillation envelope in the bifurcation plot stretches to span the range 70–165 V at  $I_0 = 30$  mA. Once  $I_0$  crosses  $\sim 30$  mA, the oscillations die down, and the bifurcation plot returns to being a single-valued curve since the winding converges to a stable steady state and remains stationary. Further increase in current results in linear increase in voltage, except for sporadic jumps, which appear whenever the electromagnetic force overcomes the limiting friction between the stationary winding and the core shaft, causing the winding to converge onto a new steady state at a greater height where the upward and downward forces balance each other out. See Supplementary Video-1 for an experimental recording of this behavior.

Oscillations occur simultaneously in mechanical, electrical, and optical domains in winding displacement, current and voltage signals, and optical intensity of the LED respectively. Figure 7c shows that the frequency of these oscillations in the oscillatory regime increases as the source current increases, and the range of frequencies observed, i.e., 4.75–7 Hz, is in agreement with the theoretical results of EOC analysis from Sect. [EOC bias conditions in an uncoupled volatile meminductor](#). Voltage oscillations shown in Fig. 7d for different source currents demonstrate the trend of increasing amplitude and frequency as  $I_0$  increases.

### Neuromorphic computing potential of the LP-coupled EOC meminductor: mimicking neuronal behaviors

In the context of nonlinear dynamical systems, the order of complexity of a system is defined as the number of first order differential equations required to completely describe its dynamical behavior<sup>53</sup>. The order of complexity in turn determines the range of dynamical responses that the system can generate and hence, plays a crucial role in designing electrical devices for bio-inspired computing applications. Biological neurons have been shown to express over 20 different dynamical behaviors based on their stimulation and activation history<sup>54</sup> and hence, mimicking neuronal behavior begins with an understanding of the specific neuronal function desired to be emulated. While primitive functions like “Integrate-and-fire” only require first-order complexity, periodic generation of action potential and “spike number adaptation” require second-order complexity as shown in Fig. 7e. Periodic bursts and chaotic oscillations require third order complexity, and hyperchaotic oscillations, fourth. Such dependence of dynamics on device complexity leads to application specific device configurations<sup>55–57</sup>.

The second order differential Eq. (13) describing the state function of an uncoupled volatile meminductor can be broken down into two first order differential equations as

$$\begin{bmatrix} \dot{x} \\ \dot{y} \end{bmatrix} = \begin{bmatrix} y \\ \frac{K_1}{m_T} \mu(x) \left( \frac{i}{x^4} \right) - \frac{k_a}{m_T} y - g \end{bmatrix}, \quad (33)$$

where  $\dot{x} \triangleq dx/dt$ . Hence, the uncoupled meminductor has a second-order complexity with its two state variables being displacement ( $x$ ) and velocity ( $y \triangleq \dot{x}$ ). Since both the state variables are volatile, the meminductor can be used to mimic only neuronal properties but not synaptic properties since the latter requires at least one state variable to result in non-volatile memory. A constant current excitation resulting in persistent periodic oscillatory behavior in voltage as shown in each panel in Fig. 7d is similar to neurons generating a periodic action potential when stimulated by a DC voltage. Further, the panels also show that increasing the input DC current level increases the frequency of resulting voltage oscillations. This property mimics “spike number adaptation”, i.e., modulation of the frequency of action potential generation by varying the input stimulus level. Dynamical behavior corresponding to higher orders of complexity such as periodic bursts and chaotic oscillations may also be potentially realized by adding more state variables to the system either in the meminductor design or by connections to appropriate coupling networks.

Due to static friction between the winding and the shaft across which it moves, it is possible to bring the winding to rest at a steady state which has been destabilized by appropriate LP coupling (Supplementary Video-3). Once so biased at a steady state, the winding does not possess the ability to self-oscillate since infinitesimal input current fluctuations cannot produce a fluctuation in the electromagnetic force large enough to overcome the limiting friction. Hence, at a given steady state, there exists a minimum current/position fluctuation threshold above which the winding starts to oscillate due to fluctuations being amplified and below which the fluctuations are damped. Thus, the meminductive oscillator not only restricts the range of input currents  $I_0$  that can result in oscillations, but also implicitly adds a thresholding feature that limits fluctuation levels  $\delta i$  that are amplified about each  $I_0$ . Such thresholding may once again be used to mimic neuronal firing behavior. Generating persistent dynamics by externally inducing position fluctuations has been recorded and presented in Supplementary Video-3.

### Conclusions

It has been shown that a meminductor biased at the edge of chaos, when connected to an appropriate coupling network, can display persistent dynamical behaviors in response to a DC current input. The state variable range resulting in persistent dynamics when a volatile meminductor is connected to a passive network has been shown to agree with the range theoretically predicted using the uncoupled element’s small-signal linearized

model. Similarities in dynamic response of the meminductor oscillator to neuronal functions such as action potential generation and spike number adaptation have been discussed thus highlighting the potential for use of meminductors in bio-computing and neuromorphic applications. Also, the necessity of circuit elements with state-dependent electrical characteristics, i.e., mem-elements, for EOC bias possibility and resultant complexity has been discussed, thus reiterating the importance of memristors, memcapacitors, and meminductors in developing neuromorphic computing architectures.

For the sake of simplicity, static and dynamic friction between the winding and the core shaft have been omitted from the small-signal model in this work. However, given the importance of static friction in determining the minimum input fluctuation level that results in oscillations, it is necessary for future models to incorporate friction along with drag force to accurately predict the system's self-oscillation capabilities and dynamical response. Design parameters for expanding EOC operation regime have been outlined and future work planned includes efforts to improve the meminductor design based on these strategies. The choice of the LP coupling network used in this work is by no means unique, and efforts to design coupling configurations more robust to parametric variations are currently being pursued. The results presented reinforce the concept that meminductors can mimic neuronal functionality, and development of nanoscale, high frequency meminductors that do not rely on macroscopic physical motion could have crucial applications in real neuromorphic hardware development.

## Data availability

The datasets used and/or analyzed during the current study are available from the corresponding author on reasonable request.

Received: 10 December 2024; Accepted: 17 July 2025

Published online: 19 November 2025

## References

1. Chua, L. O. & Kang, Sung Mo. Memristive devices and systems. *Proc. IEEE*. **64**, 209–223 (1976).
2. Di Ventra, M., Pershin, Y. V. & Chua, L. O. Circuit elements with memory: Memristors, memcapacitors, and meminductors. *Proc. IEEE*. **97**, 1717–1724 (2009).
3. Zhang, W. et al. Neuro-inspired computing chips. *Nat. Electron.* **3**, 371–382 (2020).
4. Sangwan, V. K. & Hersam, M. C. Neuromorphic nanoelectronic materials. *Nat. Nanotechnol.* **15**, 517–528 (2020).
5. Hong, X. L. et al. Oxide-based RRAM materials for neuromorphic computing. *J. Mater. Sci.* **53**, 8720–8746 (2018).
6. Choi, S., Yang, J. & Wang, G. Emerging memristive artificial synapses and neurons for energy-efficient neuromorphic computing. *Adv. Mater.* **32**, 2004659 (2020).
7. Corti, E. et al. Resistive Coupled VO<sub>2</sub> Oscillators for Image Recognition. *IEEE International Conference on Rebooting Computing, ICRC 2018* (2019). (2019). (2018).
8. Sun, K., Chen, J. & Yan, X. The future of memristors: Materials engineering and neural networks. *Adv. Funct. Mater.* **31**, 2006773 (2021).
9. Li, Z., Tang, W., Zhang, B., Yang, R. & Miao, X. Emerging memristive neurons for neuromorphic computing and sensing. *Sci. Technol. Adv. Mater.* **24**, 83 (2023).
10. Brown, T. D. et al. Electro-thermal characterization of dynamical VO<sub>2</sub> memristors via local activity modeling. *Adv. Mater.* <https://doi.org/10.1002/adma.202205451> (2022).
11. Kumar, S., Strachan, J. P. & Williams, R. S. Chaotic dynamics in nanoscale NbO<sub>2</sub> Mott memristors for analogue computing. *Nature* **548**, 318–321 (2017).
12. Strukov, D. B., Snider, G. S., Stewart, D. R. & Williams, R. S. The missing memristor found. *Nature* **453**, 80–83 (2008).
13. Wang, Z., Kumar, S., Nishi, Y. & Wong, H. S. P. Transient dynamics of NbO<sub>x</sub> threshold switches explained by Poole-Frenkel based thermal feedback mechanism. *Appl. Phys. Lett.* **112**, 193503 (2018).
14. Kumar, S. & Williams, R. S. Separation of current density and electric field domains caused by nonlinear electronic instabilities. *Nat. Commun.* **9**, 1–9 (2018).
15. Aguirre, F. et al. Hardware implementation of memristor-based artificial neural networks. *Nat. Commun.* **15**, 1–40 (2024).
16. Yi, S., Kendall, J. D., Williams, R. S. & Kumar, S. Activity-difference training of deep neural networks using memristor crossbars. *Nat. Electron.* **6**, 45–51 (2023).
17. Najem, J. S. et al. Dynamical nonlinear memory capacitance in biomimetic membranes. *Nat. Commun.* **10**, 3239. <https://doi.org/10.1038/s41467-019-11223-8> (2019).
18. Dinavahi, A., Yamamoto, A. & Harris, H. R. Physical evidence of meminductance in a passive, two-terminal circuit element. *Sci. Rep.* **13**, 1–10 (2023).
19. Demasius, K. U., Kirschen, A. & Parkin, S. Energy-efficient memcapacitor devices for neuromorphic computing. *Nat. Electron.* **4**, 748–756 (2021).
20. Chua, L. O. & CNN A vision of complexity. *Int. J. Bifurcat. Chaos*. **07**, 2219–2425 (1997).
21. Chua, L. If it's pinched it's a memristor. *Semicond. Sci. Technol.* **29**, 104001 (2014).
22. Chua, L. O. Passivity and complexity. *IEEE Transactions on Circuits and Systems I: Fundamental Theory and Applications* **46**, 71–82 (1999).
23. Itoh, M. & Chua, L. O. Memristor oscillators. *Int. J. Bifurcat. Chaos*. **18**, 3183–3206 (2008).
24. Yi, W. et al. Biological plausibility and stochasticity in scalable VO<sub>2</sub> active memristor neurons. *Nat. Commun.* **9**, 1–10 (2018).
25. Williams, R. S. What's next? *Comput. Sci. Eng.* **19**, 7–13 (2017).
26. Kim, M. K., Park, Y., Kim, I. J. & Lee, J. S. Emerging materials for neuromorphic devices and systems. *iScience* <https://doi.org/10.1016/j.isci.2020.101846> (2020).
27. Li, Y., Wang, Z., Midya, R. & Xia, Q. Joshua yang, J. Review of memristor devices in neuromorphic computing: materials sciences and device challenges. *J. Phys. D Appl. Phys.* **51**, 503002 (2018).
28. Krestinskaya, O., James, A. P. & Chua, L. O. Neuromemristive circuits for edge computing: A review. *IEEE Trans. Neural Netw. Learn. Syst.* **31**, 4–23 (2020).
29. Marković, D., Mizrahi, A., Querlioz, D. & Grollier, J. Physics for neuromorphic computing. *Nat. Rev. Phys.* **2**, 499–510 (2020).
30. Kendall, J. D. & Kumar, S. The building blocks of a brain-inspired computer. *Appl. Phys. Rev.* **7**, 96 (2020).
31. Eshraghian, J. K., Ho-Ching Iu, H. & Zhigang Wang, F. Beyond memristors: neuromorphic computing using meminductors. *Micromachines* **2023**, **14**, 486 (2023).

32. Mannan, Z. I., Choi, H., Rajamani, V., Kim, H. & Chua, L. Chua corsage memristor: phase portraits, basin of attraction, and coexisting pinched hysteresis loops. (2017). <https://doi.org/10.1142/S0218127417300117> 27.
33. Brown, T. D., Kumar, S. & Williams, R. S. Physics-based compact modeling of electro-thermal memristors: Negative differential resistance, local activity, and non-local dynamical bifurcations. *Appl. Phys. Rev.* **9**, 85 (2022).
34. Messaris, I. et al. NbO<sub>2</sub> -Mott memristor: A circuit- theoretic investigation. *IEEE Trans. Circ. Syst. I: Regul. Pap.* **68**, 4979–4992 (2021).
35. Chua, L. O. *Introduction to nonlinear network theory* (McGraw-Hill, 1969).
36. Abdelouhab, M. S., Lozi, R., Chua, L. & Memfractance, A mathematical paradigm for circuit elements with memory. *Int. J. Bifurcat. Chaos* **24**, 85 (2014).
37. Chua, L. Everything you wish to know about memristors but are afraid to ask. *Radioengineering* **24**, 319 (2015).
38. Ascoli, A. et al. On local activity and edge of chaos in a NaMLab memristor. *Front. Neurosci.* <https://doi.org/10.3389/fnins.2021.651452> (2021).
39. Brown, T. D. et al. *Electro-Thermal Characterization of Dynamical VO<sub>2</sub> Memristors via Local Activity Modeling*.
40. Mainzer, K. & Chua, L. *Local Activity Principle* (Imperial College, 2012).
41. Mainzer, K. *Chaos, CNN, Memristors and Beyond* (World Scientific, 2012).
42. Chua, L. O. Local activity is the origin of complexity. *Int. J. Bifurc. Chaos* vol. 15 www. (2005). [worldscientific.com](http://worldscientific.com)
43. Weiher, M. et al. Pattern formation with locally active S-type NbO<sub>x</sub> memristors. *IEEE Trans. Circ. Syst. I: Regul. Pap.* **66**, 2627–2638 (2019).
44. Chua, L.O. The chua lectures: from memristors and cellular nonlinear networks to the edge of chaos. 3 (2020)
45. Schill, R. A. General relation for the vector magnetic field of a circular current loop: A closer look. *IEEE Trans. Magn.* **39**, 961–967 (2003).
46. Lee, H. & 'addaxis', M. A. T. L. A. B. Central File Exchange. (2022). <https://www.mathworks.com/matlabcentral/fileexchange/9016-addaxis>
47. Thynng, K. M., Greene, C. A., Hetland, R. D., Zimmerle, H. M. & DiMarco, S. F. True colors of oceanography: Guidelines for effective and accurate colormap selection. *Oceanography* **29**, 9–13 (2016).
48. Corinto, F., Forti, M. & Chua, L. O. Nonlinear circuits and systems with memristors. *Nonlinear Circuits Syst. Memristors* (2021).
49. Gibson, G. A. Designing negative differential resistance devices based on self-heating. *Adv. Funct. Mater.* **28**, 1704175 (2018).
50. Gibson, G. A. et al. An accurate locally active memristor model for S-type negative differential resistance in NbO<sub>x</sub>. *Appl. Phys. Lett.* **108**, 23505 (2016).
51. Wang, Z., Kumar, S., Williams, R. S., Nishi, Y. & Wong, H. Intrinsic limits of leakage current in self-heating-triggered threshold switches. *Appl. Phys. Lett.* **114**, 85 (2019).
52. Reenstra, A. L. A. & Low-Frequency Oscillator using PTC and NTC thermistors. *IEEE Trans. Electron. Devices* **16**, 544–554 (1969).
53. Kumar, S., Wang, X., Strachan, J. P., Yang, Y. & Lu, W. D. Dynamical memristors for higher-complexity neuromorphic computing. *Nat. Rev. Mater.* **7**, 575–591 (2022).
54. Izhikevich, E. M. Which model to use for cortical spiking neurons? *IEEE Trans. Neural Netw.* **15**, 1063–1070 (2004).
55. Sebastian, A. et al. Temporal correlation detection using computational phase-change memory. *Nat. Commun.* **8**, 1–10 (2017).
56. Zidan, M. A., Jeong, Y. J. & Lu, W. D. Temporal learning using Second-Order memristors. *IEEE Trans. Nanotechnol.* **16**, 721–723 (2017).
57. Kumar, S., Williams, R. S. & Wang, Z. Third-order nanocircuit elements for neuromorphic engineering. *Nature* **585**, 518–523 (2020).

## Author contributions

A.D. conducted the experimental research, collected and analyzed data, and drafted the manuscript under the guidance of H.R.H. All experiments and scientific discovery was organized and managed by H.R.H. Initial manuscript was written by A.D., with significant modifications made by H.R.H.

## Declarations

### Competing interests

The authors declare no competing interests.

### Additional information

**Supplementary Information** The online version contains supplementary material available at <https://doi.org/10.1038/s41598-025-12529-y>.

**Correspondence** and requests for materials should be addressed to A.D. or H.R.H.

**Reprints and permissions information** is available at [www.nature.com/reprints](http://www.nature.com/reprints).

**Publisher's note** Springer Nature remains neutral with regard to jurisdictional claims in published maps and institutional affiliations.

**Open Access** This article is licensed under a Creative Commons Attribution-NonCommercial-NoDerivatives 4.0 International License, which permits any non-commercial use, sharing, distribution and reproduction in any medium or format, as long as you give appropriate credit to the original author(s) and the source, provide a link to the Creative Commons licence, and indicate if you modified the licensed material. You do not have permission under this licence to share adapted material derived from this article or parts of it. The images or other third party material in this article are included in the article's Creative Commons licence, unless indicated otherwise in a credit line to the material. If material is not included in the article's Creative Commons licence and your intended use is not permitted by statutory regulation or exceeds the permitted use, you will need to obtain permission directly from the copyright holder. To view a copy of this licence, visit <http://creativecommons.org/licenses/by-nc-nd/4.0/>.

© The Author(s) 2025